Electrochimica Acta 511 (2025) 145415

Contents lists available at ScienceDirect

Electrochimica Acta

journal homepage: www.journals.elsevier.com/electrochimica-acta

Amphiphilic salts as single-component, solvent-free, lithium electrolytes

Jiacheng Liu, Marvin Diaz-Segura, A. Scott Manning, Lingyu Yang, Govinda Devkota, Sunil P. Upadhyay, Jonathan K. Whitmer *, Jennifer L. Schaefer *

Department of Chemical and Biomolecular Engineering, University of Notre Dame, Notre Dame, IN 46556, USA

ARTICLE INFO

Keywords:
Electrolyte
Molten salt
Ionic liquid crystal

ABSTRACT

Electrolytes with enhanced thermal stability are sought for next-generation lithium batteries. In this work, we discuss the synthesis, thermal properties, morphology, and ionic conductivity of single-component, solvent-free electrolytes composed of lithium salts with amphiphilic anions. These salts exhibit nanoscale phase segregation between the ionic domains and aliphatic tails of the amphiphilic anions. It is found that for a series of lithium salts with a decane tail, the ionic conductivity is correlated with ion pair binding energy. The ionic conductivity is highest for the decane tailed salt with the –sulfonyl(trifluoromethanesulfonyl)imide head group (LiC10TFSI) at 5.6×10^{-7} S/cm at 70 °C, with salts with – sulfonyl(phenylsulfonyl)imide and –sulfonylazanide anions exhibiting lower conductivity. A salt with an octadecane tail and TFSI headgroup (LiC18TFSI) has further improved ionic conductivity, 4 to 1000 times higher depending on the temperature and 3.6×10^{-5} S/cm at 70 °C. LiC18TFSI is a smectic ionic liquid crystal at intermediate temperatures as confirmed through X-ray scattering experiments and molecular dynamics simulations, whereas LiC10TFSI is suspected to be a disordered ionic liquid at the measurement conditions, highlighting the importance of ionic aggregate morphology on bulk ionic conductivity of electrolytes with ion clusters.

1. Introduction

Technology in the modern world necessitates long-lived, high charge capacity batteries for applications from automobiles to pacemakers. New developments in personalized electronic devices and robotics additionally demand fast charging and discharging, safe operation, and pliable geometries [1,2]. In many of these applications, the prevailing batteries utilize aprotic liquid lithium-ion electrolytes composed of lithium salts dissolved in a mixture of organic carbonate solvents. The electrolyte liquids are volatile organic compounds; the solvent combustion during a failure event can lead to thermal runaway and explosion, and these compounds can exhibit significant reactivity with lithium metal which limits their use in beyond-lithium-ion battery designs employing lithium metal anodes [3]. Also, both Li^+ and the counter-anion are mobile in the conventional liquid electrolytes and the lithium transference number is low, resulting in performance which is limited by internal impedance from anion polarization and side-reaction of the anions on the electrodes.

Alternative electrolytes with lower flammability and lithium transference numbers near unity (so-called 'single-ion conductors') are being researched worldwide. Inorganic electrolytes can present fast ion mobility in concert with high modulus and thermal stability [4]. Nonetheless, difficulties in manufacturing, sensitivity to moisture, and brittleness have slowed their application [2]. Alternatively, single-ion conducting polymer electrolytes have better compatibility with electrodes and are amenable for low-cost industrial-scale processing [1,5,6]. However, dry single-ion conducting polymer electrolytes demonstrated thus far have ionic conductivity that is too low for most applications, with the best reported values of Li^+ conductivity of $>1 \times 10^{-4}$ S/cm at 60–90 °C achieved with ionomers containing highly dissociable bound anions in contact with poly(ethylene oxide) (PEO) chain segments through either copolymerization or blending [1,5,7]. The ionic conductivity in these PEO-based single-ion conducting polymers is dependent upon the segmental relaxation rate of the polymer chains solvating Li^+, the ion pair binding energy, and the interaction of the bound anionic site with the cation-solvating PEO. The reduction of ion clustering and excellent mixing between the ionic groups and polar polymer segments results in the highest bulk ionic conductivity in these systems.

Molecular dynamics (MD) simulations have been used to probe novel conduction mechanisms in single-ion conducting polymers. For systems lacking additional solvent or cation-solvating groups beyond the polymerized anions (i.e., lacking a polar polymer matrix such as PEO), MD

* Corresponding authors.
E-mail addresses: jwhitme1@nd.edu (J.K. Whitmer), Jennifer.L.Schaefer.43@nd.edu (J.L. Schaefer).

https://doi.org/10.1016/j.electacta.2024.145415
Received 17 August 2024; Received in revised form 11 November 2024; Accepted 23 November 2024
Available online 26 November 2024

simulations have revealed different types of Li^+ transport mechanisms: 1) structural relaxation-coupled transfer between nearby ion clusters, and 2) fast hopping of ions within an ionic cluster, potentially providing superionic conductivity [8–13]. The rate of the simulated fast ion hopping is significantly higher than the structural relaxation rate of the polymer, which could lead to a conductivity decoupled from mechanical properties of the ion-conducting phase [14–19]. Several lithiated polymers with segregated ion clusters have recently been reported [14, 20–26]. Yet, the morphological control to remove grain boundaries and afford total percolation of the ion clusters has been difficult to achieve experimentally, inhibiting the fundamental study of the ion transport within these dense ionic domains.

In this study, we investigate the potential of amphiphilic lithium salts as single-component, solvent-free electrolytes. We hypothesized that these amphiphilic lithium salts may serve as a model system and small-molecule analogs of single-ion conducting polymer electrolytes with liquid crystalline (LC) character recently reported where the ions exist in dense ionic domains with long-range periodic arrangement but there is a lack of atomic-scale crystalline order in either the polymer repeat segments or ion clusters [20,24,25]. The chemical environment of the lithium cation in the pure amphiphilic lithium salt and the corresponding ionomer with segregated ionic phases may be similar. Amphiphilic salts are known to support thermotropic liquid crystalline phases with long-range order [27–33]. In a pure salt or single-component electrolyte, long-range concentration polarization of the ions in an electric field would not be possible, due to maintenance of electroneutrality. In addition, from a practical standpoint, the amphiphilic lithium salts are easier to synthesize and expected to have lower viscosity than the polymer, which would enhance electrolyte-electrode contact.

The amphiphilic salts in this study contain sulfonylimide-derived anionic chemistries, while the cation is Li^+, a relatively hard cation with small ionic volume (see Fig. 1). Three salts are prepared with decyl tails and varying anions, lithium (decylsulfonyl)(trifluoromethanesulfonyl)imide (LiC10TFSI), lithium (decylsulfonyl)(phenylsulfonyl)imide (LiC10PSI), and lithium (decylsulfonyl)(cyano)imide (LiC10SA). The TFSI anion, commonly used in single-ion conducting polymer electrolytes, has relatively high charge delocalization. Modifications are made to this anion to change the effects of electron conjugation and anion size [34]. In the LiC10PSI, the trifluorosulfonyl group was replaced by a phenylsulfonyl group that has slightly lower charge delocalization but larger size than the trifluorosulfonyl. In the LiC10SA, the trifluorosulfonyl group was replaced by a cyano group. This cyano group has smaller size than the trifluorosulfonyl and further reduced electron delocalization. Additionally, we investigated the influence of tail length by preparing lithium (octadecylsulfonyl)(trifluoromethanesulfonyl)imide (LiC18TFSI). We note that the LiC_nTFSI salts LiC8TFSI, LiC12TFSI, and LiC16TFSI were reported over two decades ago, however limited characterization was performed on the pure materials and rather they were mixed with PEO to prepare polymer electrolytes that were then studied [35]. Here, the thermal, conduction, and structural properties of these single-component electrolytes were investigated.

2. Materials and methods

Detailed synthesis information is provided in the Supporting Information. ^1H nuclear magnetic spectroscopy (NMR) was recorded on a Bruker AVANCE III HD 400MHz Nanobay spectrometer with scan number of 16. Lithium content was assessed using inductively coupled plasma optical emission spectroscopy (ICP-OES) via a Perkin Elmer Optima 8000 ICP-OES with Prep3. Differential scanning calorimetry (DSC) was used to profile the thermal transitions of each ionic molecule. A DSC Q2000 TA Instruments was applied at a heating or cooling rate of 10 °C/min with a N_2 purge flow of 50 mL/min. Samples were cooled from room temperature to -50 °C, heated to 250 °C, held isothermally for 10 minutes at 250 °C, and then cooled back to -50 °C. Dielectric spectroscopy was performed on a Novocontrol broadband dielectric spectrometer coupled with an alpha-A high performance frequency analyzer in the range of 0.1 Hz to 1 MHz with an alternating current (AC) amplitude of 0.3 V from high to low frequency in order to extract the bulk ionic conductivity of the samples. Tested material in the liquid state was placed on a gold plated electrode and another electrode was placed on the top. The interelectrode distance was maintained with several 50 μm thick glass fibers. Samples were first heated to the highest measured temperature and then the measurement was recorded upon cooling. The samples were stabilized at each temperature for 5 mins before the dielectric measurement. Direct current (DC) ionic conductivity was determined at the frequency where the real conductivity curve plateaus. Small and wide angle X-ray scattering (SAXS-WAXS) experiments were conducted at Advanced Photon Source Synchrotron beamline 12-ID-B operated by the Chemical and Materials Science group at Argonne National Laboratory. The wavelength of the X-ray beam was 0.9322 Å corresponding to 13.3 keV, and the exposure time was 0.1 sec. The cooling rate was set to 10 °C/min, and the cooling was paused at each measurement temperature for several minutes for data collection.

Molecular dynamics simulations using GROMACS 2018.3[36,37] (input files provided in the SI) were prepared starting from a presumed crystal structure for 512 ion pairs placed into two layers. For this state, it is presumed lithium cations are arranged next to the anionic headgroups, and tail groups interdigitate. This configuration remains relatively stable until the layers melt into a smectic state at elevated temperature. We utilized Avogadro 1.2.0[38,39] for initial molecular topology generation, and built the molecular model atop the GAFF2[40] forcefield with antechamber 22.0[41] optimization for missing terms and partial charges. The partial charges were then scaled by 0.7 using standard protocols. The general protocol utilized energy minimization to relax large forces, subsequent equilibration at constant pressure and temperature (initially 300 K) using a v-rescale thermostat,[42] with first a semi-isotropic Berendsen barostat at 1 bar pressure and then an

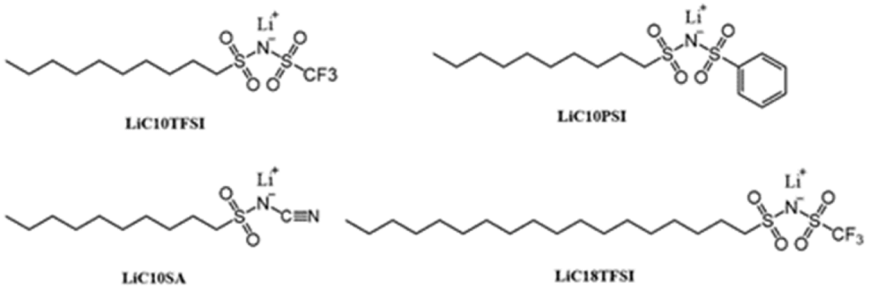

Fig. 1. Molecular structures of amphiphilic lithium salts in this study. Their molecular lengths as estimated through ChemDraw 3D software under the assumption of a fully extended aliphatic chain as detailed in the Supporting Information (**Figures S1–4**) are as follows: LiC10TFSI (16.8 Å), LiC10PSI (17.9 Å), LiC10SA (15.3 Å), and LiC18TFSI (26.9 Å).

isotropic Berendsen barostat for a total of 10^7 *NPT* steps. Anisotropic coupling is necessary so that the molecular spacing in the *xy* plane can be relaxed independently from the layer spacing, which is aligned with the *z* axis. For production runs, these equilibrated configurations were coupled at the appropriate temperature to a semi-isotropic Parinello-Rahman barostat. From the initial temperature of 300 K, temperature was raised in stages, 50 K at a time, using a 10 ns equilibration period at each temperature. The output of these equilibration runs is used as the initial condition for independent Parinello-Rahman NPT simulations lasting 200 ns each, over which thermodynamic and structural data is gathered. Example initial conditions and NPT run files are provided in the supplementary information.

3. Results and discussion

3.1. Organic ionic salt molecules

The organic ionic salt molecules in this study (shown in Fig. 1) resemble ionic liquids (ILs) with respect to physical properties. While an ionic liquid could refer to any ionic compound exhibiting liquid-like properties, the term IL is generally used to refer to salt species whose melting temperature is below 100 °C, with species having higher melting temperatures referred to as molten salts in their liquid phase. ILs are typically composed of a cation and anion pairs where at least one species is significantly larger than simple metal ions, having an extended structure which limits entropy in crystallization, and whose charge is relatively less localized than in simple metal ions [43].

Here, in order to prevent crystallization of the ionic head groups and promote the LC phase, the anions in this study are derivitized with a hydrocarbon tail with either 10 or 18 methylene (and methyl) groups. The synthesis strategy of the organic ionic salts was adopted from prior works and modified to result in different tethered anionic groups [35, 44]. The synthesis route, as depicted in Fig. 2, begins with the precursor 1-bromodecane for LiC10TFSI, LiC10SA, and LiC10PSI, and sodium octadecanesulfonate for LiC18TFSI. The molecules with a C10-tail are obtained with a 4-step synthesis procedure, that may be shortened by using sodium decanesulfonate as the starting material. LiC18TFSI is achieved in 3 steps with high yield at each step. The nucleophilic effect of the cyanamide is lower than its companions, which causes the yield of the LiC10SA to be lower than the others. All four molecules can be readily obtained by precipitation in low polarity solvent after the lithiation reaction. They are powdery solids at room temperature after drying in the vacuum oven. Their solubility in non-polar organic solvent is negligible while they are soluble in high polarity solvents such as dimethylformamide (DMF), alcohols, and water. Their solubility suggests that the electrostatic interactions within the ion-pairs is strong. Meanwhile, the C10-tailed molecules are visually hygroscopic in the atmosphere suggesting their high hydrophilicity. On the contrary, the LiC18TFSI is not as hygroscopic in the atmosphere, due to the longer hydrophobic tail.

The ^{1}H NMR spectra of the three C10 salts are presented in Fig. 3, while complete ^{1}H NMR analysis confirming successful synthesis of the target molecules is provided in the Supporting Information (**Figures S5-S8**). The peak of protons adjacent to the sulfonyl groups are denoted. Their chemical shifts are 2.93, 2.85, and 2.77 ppm, for -TFSI$^-$, -PSI$^-$, and -SA$^-$, respectively. The electron-delocalizing effect of each anion is reflected in the above chemical shifts, as increased electronegativity of the functional group (X) adjacent to the protons of the -CH_2X moiety will cause the chemical shift of those protons to move down field (increase in ppm). The -TFSI$^-$ has the highest delocalizing effect while the -SA$^-$ presents the lowest [45].

3.2. Differential scanning calorimetry

In Fig. 4, differential scanning calorimetry (DSC) traces of each molecule are presented. Untreated powder samples directly after the

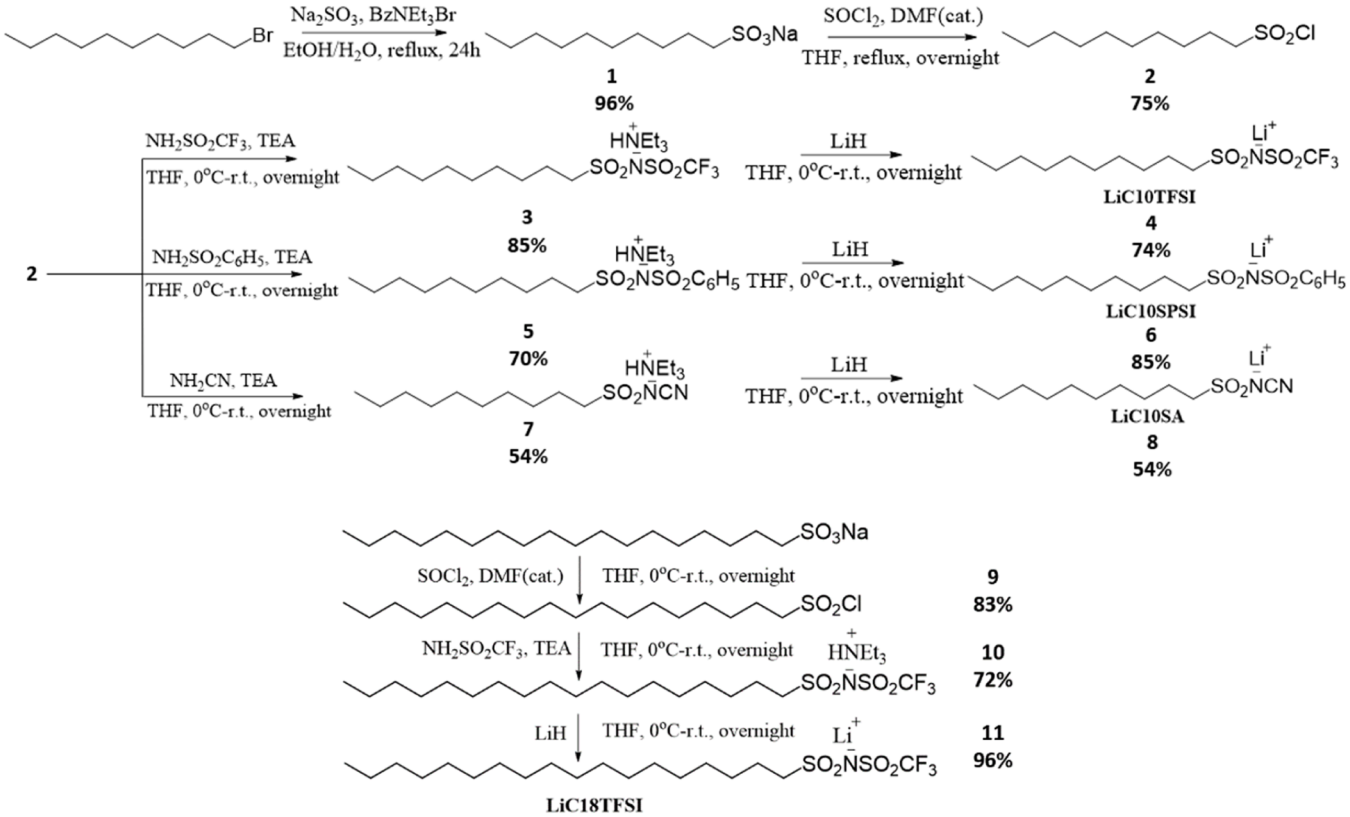

Fig. 2. Synthesis scheme of LiC10TFSI, LiC10PSI, LiC10SA, and LiC18TFSI, including yields for each product.

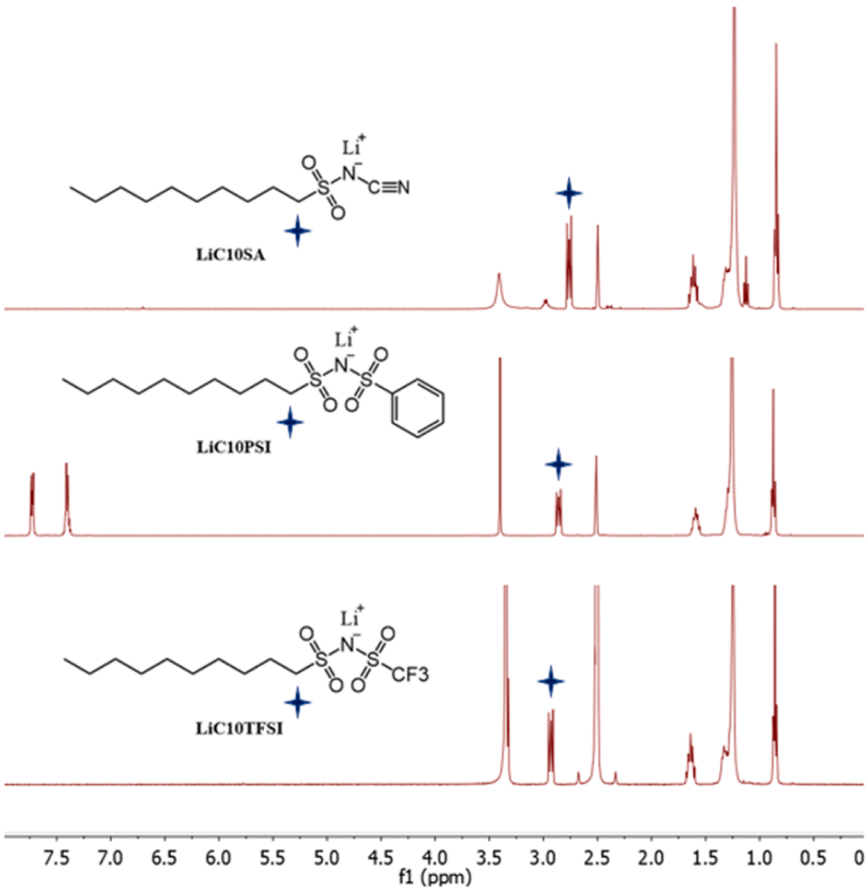

Fig. 3. ^{1}H NMR of LiC10TFSI, LiC10PSI, and LiC10SA in DMSO-d_6.

chemical synthesis and drying are subjected to cooling to -50 °C, then heating to 250 °C, then an isothermal hold, and finally another cooling ramp. The heating and second cooling ramps are shown.

For LiC10SA (Fig. 4 **a**), endothermic peaks associated with melting are present at 94 °C and 142 °C upon heating. After the isothermal hold, no exothermic events are observed upon cooling. Gradual slope changes that may be indicative of a glass transition are present at low temperatures on both heating and cooling runs. The data indicates that the time required for crystallization is greater than that available during the cooling run before glass formation occurs. Additionally, glass and crystalline phases of LiC10SA may coexist with certain environmental history (like that during the sample preparation prior to the heating run). Turning next to LiC10PSI (Fig. 4 **b**), endothermic peaks are found at 98 °C and 107 °C, indicating closely occurring melting events. Again, no exothermic events are observed upon cooling.

For LiC10TFSI (Fig. 4 **c**), upon heating a significant endothermic peak occurs at 100 °C that is attributed to melting. Upon further heating, a small exothermal event occurs at 149 °C. After the isothermal hold, a small endothermic peak at 249 °C and then a small exothermic peak appears at 145 °C upon cooling. The low intensity of the three thermal events above 125 °C suggests that they could be related to LC-to-LC and/or LC-to-isotropic phase transitions [46]. The existence of two low intensity thermal events in the cooling scan implies the existence of at least two different LC phases present during this scan. There is no additional exothermic event upon further cooling of the sample during the DSC measurement.

A distinct thermal behavior was found for LiC18TFSI. As shown in Fig. 4 **d**, narrow peaks are observed on both heating and cooling ramps. Upon heating, a melting transition peaked at 67 °C, after which a cold crystallization peak happened at 79 °C and then another significant melting peak at 107 °C. A small exothermic event occurred at 197 °C. After the isothermal hold, a small exothermic peak appears at 193 °C upon cooling. Again, the low intensity thermal events at higher temperatures are likely to be associated with LC-to-LC or LC-to-isotropic phase transitions. Finally, further cooling results in a significant crystallization peak at 62 °C. The longer hydrocarbon tail for LiC18TFSI, versus LiC10TFSI, increases the ionophilic and ionophobic phase separation and enables the crystallization of the tails to happen at a faster rate, as evidenced by the existence of the significant crystallization event on the cooling scan for LiC18TFSI. Furthermore, a wide LC temperature window of 86 °C (if 193 °C is the upper bound and 107 °C is the lower bound) would be favorable for the analysis of conductivity that is affected by the ion-cluster phase.

3.3. Ionic conductivity

Ionic conductivity of the salts as measured upon cooling is shown in Fig. 5. The conductivity curves for LiC10SA and LiC10PSI are Vogel-Fulcher-Tammann (VFT) type from 180 °C to 30 °C. This functional form of the conductivity temperature dependence indicates that the conductivity is related to a relaxation process. The slow crystallization of these molecules, as confirmed by the previously discussed DSC experiments, allowed for this result. In contrast, discontinuity is observable in the conductivity collected upon cooling for LiC10TFSI and LiC18TFSI. At lower temperatures, the observed Arrhenius temperature dependent ionic conductivity implies ion hopping rather than relaxation mediated ion transport, which is typical for (semi-)crystallized and glassy ionic conductors. While LiC18TFSI showed a clear crystallization transition in DSC below 100 °C, LiC10TFSI did not. The difference in the phase change temperature observed in DSC upon cooling from the deviation from VFT behavior for the conductivity is common and can be attributed to substrate effects and differences in cooling rates between the two

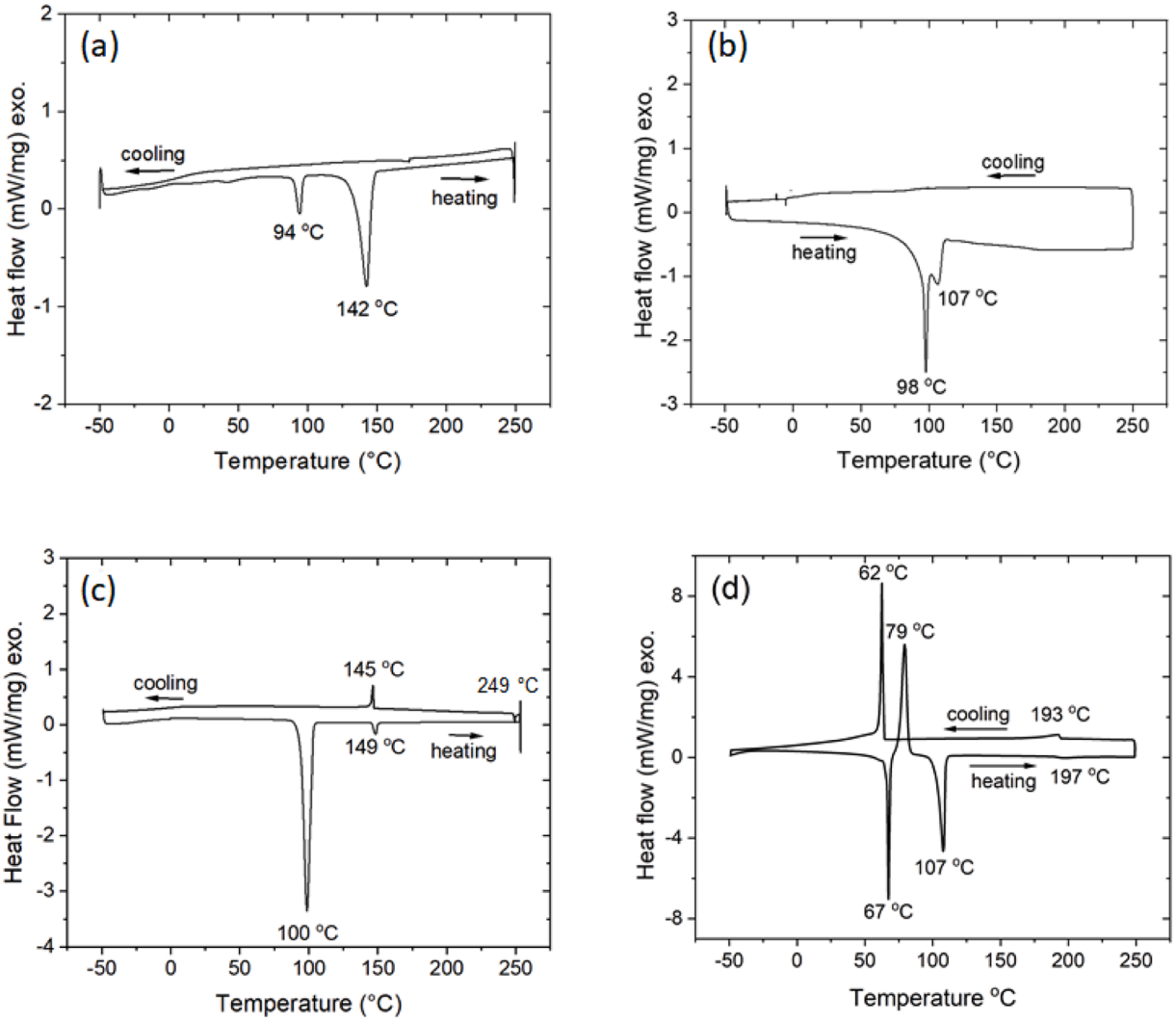

Fig. 4. DSC thermograms of (a) LiC10SA, (b) LiC10PSI, (c) LiC10TFSI, and (d) LiC18TFSI.

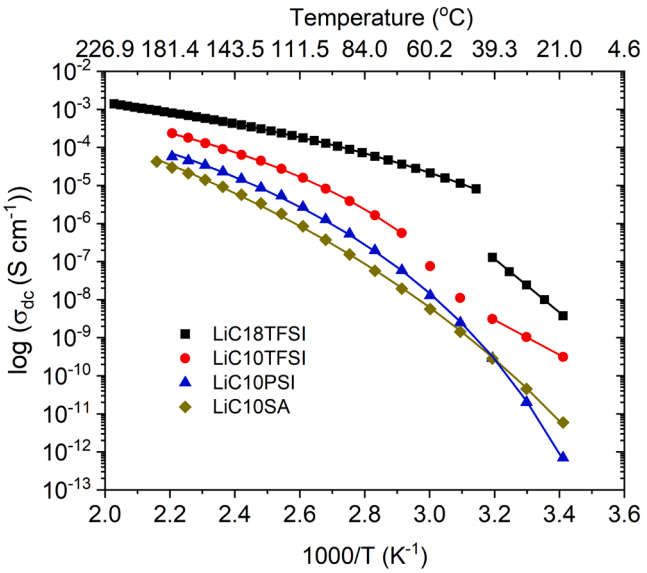

Fig. 5. Ionic conductivity data with VFT and Arrhenius fits displayed as lines.

measurements.

The conductivity of LiC10SA, LiC10PSI, and LiC10TFSI are 1.9×10^{-8} S/cm, 5.9×10^{-8} S/cm, and 5.6×10^{-7} S/cm, respectively, at 70 °C. The conductivity of the three decane-tailed materials follows the trend of higher conductivity with lower ion-pair binding energy, the same as with our previous findings for a side-chain polymer system [43]. In contrast, the reason for the difference in conductivity of LiC10TFSI and LiC18TFSI - 5.6×10^{-7} S/cm and 3.6×10^{-5} S/cm at 70 °C - is not obvious. In fact, in the absence of ion mobility differences, LiC10TFSI would be expected to have higher ionic conductivity than LiC18TFSI due to the higher ion number concentration, but the reverse trend for higher ionic conductivity with lower bulk ion concentration is found. We estimate that the molar ionic conductivity of LiC18TFSI exceeds that of LiC10TFSI at 70 °C by about 120 times. Further discussion on conductivity normalization may be found in the Supporting Information.

3.4. Morphology investigation

The phase morphology of LiC10TFSI and LiC18TFSI was investigated with small- and wide-angle X-ray scattering (SAXS-WAXS, Fig. 6) upon cooling in order to elucidate the reason for the significant difference in their ionic conductivity. Limited additional scattering experiments were performed on other samples, and this data and discussion may be found in the Supporting Information (**Figure S9**) [47].

Each LiC10TFSI and LiC18TFSI were heated to a temperature at

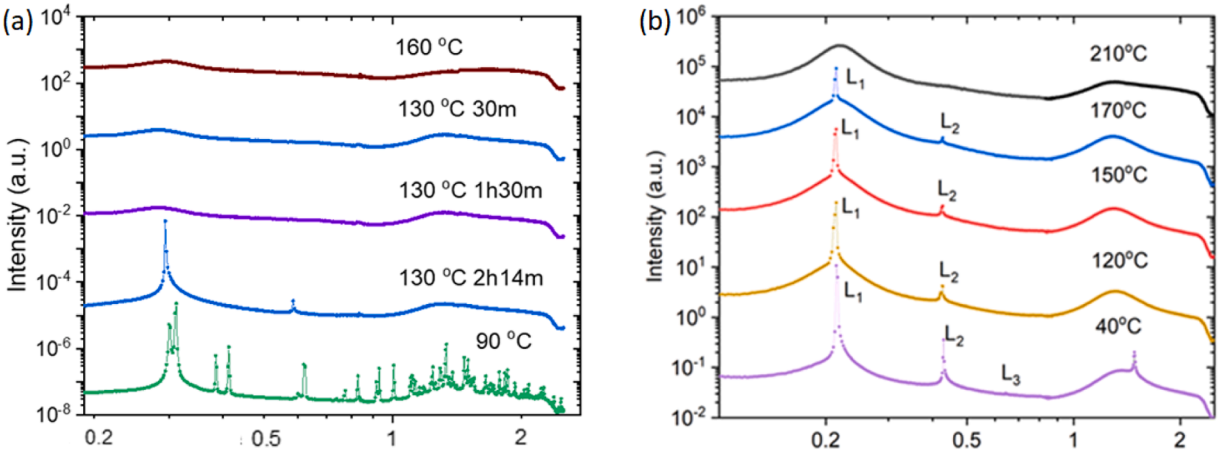

Fig. 6. SAXS-WAXS of samples (a) LiC10TFSI and (b) LiC18TFSI recorded upon cooling.

which only broad scattering features at both high q (wide angle scattering, related to short length scales) and at low q (small angle scattering, related to longer length scales) were observed. Interestingly, these broad peaks were observed for LiC10TFSI at 160 °C, a temperature above the small thermal event observed at 149 °C but below the event observed after the high temperature hold in DSC. Both the isotropic and nematic phases could result in the broad scattering, but the higher temperature DSC event implies that the isotropic phase should not be present at 160 °C upon heating. This high temperature DSC event for LiC10TFSI was confirmed via replication. However, nematic phases are rare for ionic liquid crystals. Recent coarse-grained simulations suggest that ionic liquid crystals with the charge located at the center of the mesogen may form nematics while in the amphiphilic case like we are concerned with here, the smectic is the only LC phase observed with direct transition to the isotropic [48]. Either way, whether the broad scattering in each LiC10TFSI and LiC18TFSI is from the isotropic or nematic phase, the ion clusters in those phases must be relatively disordered much like in an ionic liquid.

Upon cooling of LiC10TFSI from 160 °C to 130 °C, below the small DSC peak observed at 149 °C, there was little immediate change to the scattering profile. Close inspection reveals a change in the curvature of the amorphous halo in the wide angle region of the profile and a slight shift in the broad peak in the small angle region. At 130 °C, the broad peak in the small angle region at $q = 0.29$ Å^{-1} corresponds to a broad distribution of correlation distance of ionic groups with a mode of 2.1 nm. As ionic liquid crystals with this head-to-tail shape typically form a smectic phase that would be visible with scattering, we chose to hold the temperature at 130 °C and periodically collect scattering data to see if a morphological change was observed. Indeed, after holding at 130 °C for more than 2 hours, smectic peaks were observed with $q_1 = 0.29$ Å^{-1} and $q_2 = 2q_1 = 0.58$ Å^{-1} which correspond to a 2.1 nm layer-to-layer distance of the ionic phase. Real space distances may be related to reciprocal q space via the Bragg equation, $d = 2\pi/q$. Considering that the fully extended length of LiC10TFSI is estimated at less than 1.7 nm, the LC layer spacing could result from overlapping tails. Further cooling to 90 °C led to the hard crystal phase.

In contrast, when LiC18TFSI was cooled for scattering measurements, the phase changes were found to be spontaneous to temperature changes. At 210 °C, the broad peak at $q = 0.22$ Å^{-1} indicates an ionic correlation distance of 2.5 nm. Upon cooling to 170 °C, immediately narrow scattering peaks at $q_1 = 0.21$ Å^{-1} and $q_2 = 2q_1 = 0.43$ Å^{-1} appeared atop the broad scatter, while no narrow peaks were found in the WAXS region. The distance between nearest smectic layers was 2.9 nm, similar to the estimated extended length of the LiC18TFSI at ≈2.7 nm. With continued cooling, the smectic peaks grew in height while the disordered fraction was reduced. The same behavior persisted until the temperature was 40 °C, below the DSC crystallization temperature, where a single WAXS peak appeared that is characteristic of the hexagonal packing of alkyl chains [49–51]. LiC18TFSI exhibits a robust smectic LC phase over a wide elevated temperature range.

We also investigated the assembly of LiC18TFSI using molecular dynamics simulations. The MD simulations are performed starting from a hypothetical crystal geometry at 27 °C (300 K), which is slowly heated in stages to 227 °C (500 K). A melting transition to the smectic-like phase displayed in Fig. 7 **(a)** is observed at approximately 127 °C (400 K). While this does not correlate identically with the values observed in experiment — a common feature of simulations performed using generalized force fields which have not been optimized to match thermodynamic measurements — we may still understand structural features in the smectic phase which correlate strongly with the layering observations in Fig. 6 **(b)**. Importantly, we observe an effective layer spacing obtained as half the box length in the layered direction of $\gtrsim$3.0 nm (see Fig. 7 **(b)**), which compares favorably with the layer spacing obtained from scattering. The spacing is stable until the smectic phase begins to melt around 500 K. It is noted that similar simulations were attempted for LiC10TFSI, however only a metastable smectic phase was identified.

Based on the clear formation of a stable smectic in LiC18TFSI over a wide temperature range and increased ionic conductivity of this material relative to LiC10TFSI, we anticipate that the ionic conductivity of LiC10TFSI is limited by disorder of the ionic domains. Decreased continuity between ionic clusters must lead to a decreased rate of long-range lithium transport.

4. Conclusions

In this contribution, we have reported on amphiphilic lithium salts without Li^+ solvation functionality besides the tethered anion, that phase segregate at the nanoscale into ion-rich and hydrocarbon-rich domains. These materials may be used as model systems to study cation conduction in materials with dense ionic clusters. Through the study of various bis(sulfonylimide) anions, it is found that the decane-tailed salts with the most charge-delocalized anion studied (LiC10TFSI) exhibit the highest bulk ionic conductivity. Meanwhile, the extension of the non-polar tail to 18 carbon atoms (LiC18TFSI) results in more stable formation of the smectic liquid crystal phase and an increase in the bulk ionic conductivity of 4 to 1000 times higher compared with LiC10TFSI. The bulk ionic conductivity of LiC18TFSI at 60 °C is 2×10^{-5} S/cm, comparable to the conductivity of routine salt-doped PEO electrolytes. These results suggest that the long-range ion transport is faster in materials with ordered ion clusters compared with disordered ion clusters, perhaps due to a reduction in the concentration of cluster-

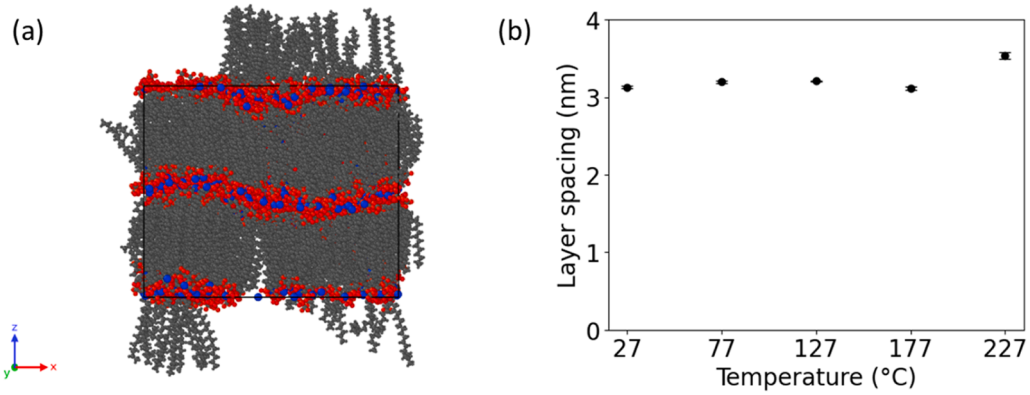

Fig. 7. (a) MD snapshot of LiC18TFSI at 400 K with layer spacing of 3.0 nm. (b) Layer spacing of LiC18TFSI with temperature increments; the observed spacing is slightly larger than what is observed in experiments but nonetheless correlates well in the smectic range. The error bars depict standard errors.

cluster boundaries.

CRediT authorship contribution statement

Jiacheng Liu: Writing – original draft, Visualization, Methodology, Investigation, Formal analysis, Data curation. **Marvin Diaz-Segura:** Writing – original draft, Visualization, Investigation, Formal analysis. **A. Scott Manning:** Investigation. **Lingyu Yang:** Visualization, Validation, Investigation. **Govinda Devkota:** Validation, Investigation. **Sunil P. Upadhyay:** Investigation. **Jonathan K. Whitmer:** Writing – review & editing, Supervision, Resources, Project administration, Methodology, Data curation. **Jennifer L. Schaefer:** Writing – review & editing, Supervision, Project administration, Methodology, Funding acquisition, Formal analysis, Conceptualization.

Declaration of competing interest

The authors declare that they have no known competing financial interests or personal relationships that could have appeared to influence the work reported in this paper.

Acknowledgements

The authors gratefully acknowledge financial support from the National Science Foundation via award number DMR-1654162, the Department of Education via grant number P200A210048, and from the University of Notre Dame (College of Engineering and the Graduate School). The authors also gratefully acknowledge Dr. Xiaobing Zuo's help at Advanced Photon Source beamline 12-ID-B at Argonne National Laboratory, the Center for Environmental Science and Technology at the University of Notre Dame for ICP-OES instrumentation, the University of Notre Dame Magnetic Resonance Center for NMR instrumentation, and Prof. Ruilan Guo's support for use of DSC instrumentation in the Department of Chemical and Biomolecular Engineering at the University of Notre Dame. This research used resources of the Advanced Photon Source, a U.S. Department of Energy (DOE) Office of Science User Facility operated for the DOE Office of Science by Argonne National Laboratory under Contract No. DE-AC02-06CH11357.

Supplementary materials

Supplementary material associated with this article can be found, in the online version, at doi:10.1016/j.electacta.2024.145415.

Data availability

Data will be made available on request.

References

[1] H. Zhang, C. Li, M. Piszcz, E. Coya, T. Rojo, L.M. Rodriguez-Martinez, M. Armand, Z. Zhou, Chem. Soc. Rev. 46 (2017) 797–815.
[2] P. Albertus, V. Anandan, C. Ban, N. Balsara, I. Belharouak, J. Buettner-Garrett, Z. Chen, C. Daniel, M. Doeff, N.J. Dudney, B. Dunn, S.J. Harris, S. Herle, E. Herbert, S. Kalnaus, J.A. Libera, D. Lu, S. Martin, B.D. McCloskey, M.T. McDowell, Y. S. Meng, J. Nanda, J. Sakamoto, E.C. Self, S. Tepavcevic, E. Wachsman, C. Wang, A. S. Westover, J. Xiao, T. Yersak, ACS Energy Lett 6 (2021) 1399–1404.
[3] H. Wang, Z. Yu, X. Kong, S.C. Kim, D.T. Boyle, J. Qin, Z. Bao, Y. Cui, Joule 6 (2022) 588–616.
[4] S. Ramakumar, C. Deviannapoorani, L. Dhivya, L.S. Shankar, R. Murugan, Prog. Mater. Sci. 88 (2017) 325–411.
[5] S. Han, P. Wen, H. Wang, Y. Zhou, Y. Gu, L. Zhang, Y. Shao-Horn, X. Lin, M. Chen, Nat. Mater. 22 (2023) 1515–1522.
[6] J. Zhu, Z. Zhang, S. Zhao, A.S. Westover, I. Belharouak, P. Cao, Adv. Energy Mater. 11 (2021) 2003836.
[7] W. Zhang, S. Feng, M. Huang, B. Qiao, K. Shigenobu, L. Giordano, J. Lopez, R. Tatara, K. Ueno, K. Dokko, M. Watanabe, Y. Shao-Horn, J.A. Johnson, Chem. Mater. 33 (2021) 524–534.
[8] D.S. Bolintineanu, M.J. Stevens, A.L. Frischknecht, ACS Macro Lett 2 (2013) 206–210.
[9] J.A. Bollinger, M.J. Stevens, A.L. Frischknecht, ACS Macro Lett 9 (2020) 583–587.
[10] B. Ma, M. Olvera De La Cruz, J. Phys. Chem. B 125 (2021) 3015–3022.
[11] L.M. Hall, M.J. Stevens, A.L. Frischknecht, Macromolecules 45 (2012) 8097–8108.
[12] M. Muthukumar, ACS Macro Lett 10 (2021) 958–964.
[13] M.J. Park, Mol. Syst. Des. Eng. 4 (2019) 239–251.
[14] L. Yan, C. Rank, S. Mecking, K.I. Winey, J. Am. Chem. Soc. 142 (2020) 857–866.
[15] C. Rank, L. Yan, S. Mecking, K.I. Winey, Macromolecules 52 (2019) 8466–8475.
[16] L.R. Middleton, K.I. Winey, Annu. Rev. Chem. Biomol. Eng. 8 (2017) 499–523.
[17] C.F. Buitrago, D.S. Bolintineanu, M.E. Seitz, K.L. Opper, K.B. Wagener, M. J. Stevens, A.L. Frischknecht, K.I. Winey, Macromolecules 48 (2015) 1210–1220.
[18] L. Yan, L. Hoang, K.I. Winey, Macromolecules 53 (2020) 1777–1784.
[19] L.J. Abbott, H.G. Buss, J.L. Thelen, B.D. Mccloskey, J.W. Lawson, Macromolecules 52 (2019) 5518–5528.
[20] M.A. Stolberg, B.A. Paren, P.A. Leon, C.M. Brown, G. Winter, K. Gordiz, A. Concellón, R. Gómez-Bombarelli, Y. Shao-Horn, J.A. Johnson, J. Am. Chem. Soc. 145 (2023) 16200–16209.
[21] J. Park, A. Staiger, S. Mecking, K.I. Winey, Macromolecules 54 (2021) 4269–4279.
[22] L. Yan, L. Hoang, K.I. Winey, Macromolecules 53 (2020) 1777–1784.
[23] B.A. Paren, B.A. Thurston, W.J. Neary, A. Kendrick, J.G. Kennemur, M.J. Stevens, A.L. Frischknecht, K.I. Winey, Macromolecules 53 (2020) 8960–8973.
[24] J. Liu, J.L. Schaefer, Macromolecules 56 (2023) 2515–2525.
[25] J. Liu, L. Yang, P.D. Pickett, B. Park, J.L. Schaefer, Macromolecules 55 (2022) 7752–7762.
[26] J. Liu, P.D. Pickett, B. Park, S.P. Upadhyay, S.V. Orski, J.L. Schaefer, Polym. Chem. 11 (2020) 461–471.
[27] K. Binnemans, Chem. Rev. 105 (2005) 4148–4204.
[28] K. Goossens, K. Lava, C.W. Bielawski, K. Binnemans, Chem. Rev. 116 (2016) 4643–4807.
[29] G. Saielli, A. Bagno, Y. Wang, J. Phys. Chem. B 119 (2015) 3829–3836.
[30] B. Soberats, M. Yoshio, T. Ichikawa, H. Ohno, T. Kato, J. Mater. Chem. A 3 (2015) 11232–11238.
[31] K. Salikolimi, A.A. Sudhakar, Y. Ishida, Langmuir 36 (2020) 11702–11731.
[32] G. Saielli, Y. Wang, J. Phys. Chem. B 120 (2016) 9152–9160.
[33] H. Shimura, M. Yoshio, K. Hoshino, T. Mukai, H. Ohno, T. Kato, J. Am. Chem. Soc. 130 (2008) 1759–1765.
[34] R. Meziane, J.-P. Bonnet, M. Courty, K. Djellab, M. Armand, Electrochim. Acta 57 (2011) 14–19.
[35] S. Béranger, M.H. Fortier, D. Baril, M.B. Armand, Solid State Ionics 148 (2002) 437–441.

[36] H. Bekker, H.J.C. Berendsen, E.J. Dijkstra, S. Achterop, R. van Drunen, D. van der Spoel, A. Sijbers and H. Keegstra, in *Physics Computing 92*, eds. R. A. de Groot and J. Nadrchal, World Scientific, Singapore, 1993.
[37] E. Lindahl, B. Hess, D. van der Spoel, J. Mol. Model. 7 (2001) 306–317.
[38] Avogadro: an open-source molecular builder and visualization tool. Version 1.2.0. http://avogadro.cc/.
[39] M.D. Hanwell, D.E. Curtis, D.C. Lonie, T. Vandermeersch, E. Zurek, G.R. Hutchison, J. Cheminform. 4 (2012) 17.
[40] J. Wang, R.M. Wolf, J.W. Caldwell, P.A. Kollman, D.A. Case, J. Comput. Chem. 25 (2004) 1157–1174.
[41] J. Wang, W. Wang, P.A. Kollman, D.A. Case, J. Mol. Graph. Model. 25 (2006) 247–260.
[42] G. Bussi, D. Donadio, M. Parrinello, J. Chem. Phys. 126 (2007) 014101.
[43] M. Armand, F. Endres, D.R. MacFarlane, H. Ohno, B. Scrosati, Nat. Mater. 8 (2009) 621–629.
[44] A.S. Shaplov, P.S. Vlasov, M. Armand, E.I. Lozinskaya, D.O. Ponkratov, I. A. Malyshkina, F. Vidal, O.V. Okatova, G.M. Pavlov, C. Wandrey, I.A. Godovikov, Y.S. Vygodskii, Polym. Chem. 2 (2011) 2609–2618.
[45] S. Farmer, D. Kennepohl, T. Soderberg, L. Reutenauer and L. Reutenauer, 13.3: Chemical Shifts in 1H NMR Spectroscopy, LibreTexts(TM) Chemistry, Available at https://chem.libretexts.org/Bookshelves/Organic_Chemistry/Organic_Chemistry_(Morsch_et_al.)/13%3A_Structure_Determination_-_Nuclear_Magnetic_Resonance_Spectroscopy/13.03%3A_Chemical_Shifts_in_H_NMR_Spectroscopy.
[46] S. Singh, Physics Reports 324 (2000) 107–269.
[47] S. Ohashi, J. Kilbane, T. Heyl, H. Ishida, Macromolecules 48 (2015) 8412–8417.
[48] C. Haege, S. Jagiella, F. Giesselmann, ChemPhysChem 24 (2023) e202200424.
[49] S. Kitphaitun, H. Takeshita, K. Nomura, ACS Omega 7 (2022) 6900–6910.
[50] L. Yan, M. Hauler, J. Bauer, S. Mecking, K.I. Winey, Macromolecules 52 (2019) 4949–4956.
[51] E.B. Trigg, T.W. Gaines, M. Maréchal, D.E. Moed, P. Rannou, K.B. Wagener, M. J. Stevens, K.I. Winey, Nat. Mater. 17 (2018) 725–731.